
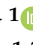

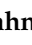



Article

Deposition of Nanosized Amino Acid Functionalized Bismuth Oxido Clusters on Gold Surfaces

Annika Morgenstern ¹, Rico Thomas ², Apoorva Sharma ¹, Marcus Weber ^{2,3} , Oleksandr Selyshchev ¹ , Ilya Milekhin ¹, Doreen Dentel ⁴, Sibylle Gemming ^{3,5} , Christoph Tegenkamp ⁴, Dietrich R. T. Zahn ^{1,3} , Michael Mehring ^{2,3,*} and Georgeta Salvan ^{1,3,*} 

¹ Semiconductor Physics, Institute of Physics, Chemnitz University of Technology, 09107 Chemnitz, Germany; annika.morgenstern@physik.tu-chemnitz.de (A.M.); apoorva.sharma@physik.tu-chemnitz.de (A.S.); oleksandr.selyshchev@physik.tu-chemnitz.de (O.S.); ilya.milekhin@physik.tu-chemnitz.de (I.M.); zahn@physik.tu-chemnitz.de (D.R.T.Z.)

² Coordination Chemistry, Institute of Chemistry, Chemnitz University of Technology, 09107 Chemnitz, Germany; rico.thomas@s2013.tu-chemnitz.de (R.T.); marcus.weber@chemie.tu-chemnitz.de (M.W.)

³ Center of Materials, Architectures and Integration of Nanomembranes, Chemnitz University of Technology, 09126 Chemnitz, Germany; sibylle.gemming@physik.tu-chemnitz.de

⁴ Solid Surface Analysis, Institute of Physics, Chemnitz University of Technology, 09107 Chemnitz, Germany; doreen.dentel@physik.tu-chemnitz.de (D.D.); christoph.tegenkamp@physik.tu-chemnitz.de (C.T.)

⁵ Theoretical Physics of Quantum Mechanical Processes and Systems, Institute of Physics, Chemnitz University of Technology, 09107 Chemnitz, Germany

* Correspondence: michael.mehring@chemie.tu-chemnitz.de (M.M.); salvan@physik.tu-chemnitz.de (G.S.)



Citation: Morgenstern, A.; Thomas, R.; Sharma, A.; Weber, M.; Selyshchev, O.; Milekhin, I.; Dentel, D.; Gemming, S.; Tegenkamp, C.; Zahn, D.R.T.; et al. Deposition of Nanosized Amino Acid Functionalized Bismuth Oxido Clusters on Gold Surfaces.

Nanomaterials **2022**, *12*, 1815. <https://doi.org/10.3390/nano12111815>

Academic Editors: Valentin Craciun, Felicia Iacomi and Romulus Tetean

Received: 5 April 2022

Accepted: 19 May 2022

Published: 26 May 2022

Publisher's Note: MDPI stays neutral with regard to jurisdictional claims in published maps and institutional affiliations.



Copyright: © 2022 by the authors. Licensee MDPI, Basel, Switzerland. This article is an open access article distributed under the terms and conditions of the Creative Commons Attribution (CC BY) license (<https://creativecommons.org/licenses/by/4.0/>).

Abstract: Bismuth compounds are of growing interest with regard to potential applications in catalysis, medicine, and electronics, for which their environmentally benign nature is one of the key factors. One thing that currently hampers the further development of bismuth oxido-based materials, however, is the often low solubility of the precursors, which makes targeted immobilisation on substrates challenging. We present an approach towards the solubilisation of bismuth oxido clusters by introducing an amino carboxylate as a functional group. For this purpose, the bismuth oxido cluster $[\text{Bi}_{38}\text{O}_{45}(\text{NO}_3)_{20}(\text{dmsO})_{28}](\text{NO}_3)_4 \cdot 4\text{dmsO}$ (dmsO = dimethyl sulfoxide) was reacted with the sodium salt of *tert*-butyloxycarbonyl (Boc)-protected phenylalanine (L-Phe) to obtain the soluble and chiral nanocluster $[\text{Bi}_{38}\text{O}_{45}(\text{Boc-Phe-O})_{24}(\text{dmsO})_9]$. The exchange of the nitrates by the amino carboxylates was proven by nuclear magnetic resonance, Fourier-transform infrared spectroscopy, as well as elemental analysis and X-ray photoemission spectroscopy. The solubility of the bismuth oxido cluster in a protic as well as an aprotic polar organic solvent and the growth mode of the clusters upon spin, dip, and drop coating on gold surfaces were studied by a variety of microscopy, as well as spectroscopic techniques. In all cases, the bismuth oxido clusters form crystalline agglomerations with size, height, and distribution on the substrate that can be controlled by the choice of the solvent and of the deposition method.

Keywords: Boc-protected amino acid functionalized chiral bismuth oxido nanocluster; spin coating; dip coating; drop coating; FTIR; XPS; optical microscopy; SEM; AFM; film growth mechanisms

1. Introduction

The environmentally benign nature of bismuth compounds offers access to novel sustainable materials and led to developments, e.g., in catalysis, medicine, radiopaque additives, and electronics [1–12]. Among the starting materials used for the synthesis of solid-state materials, bismuth(III) nitrate pentahydrate is one of the most common and readily available compounds. However, it shows poor solubility in all kinds of solvents, and easily hydrolyses to give various condensation products, of different stoichiometry and nuclearity [13–15]. These so-called bismuth subnitrates were recently studied in order to elucidate the molecular mechanisms of the condensation that lead to the formation of bismuth

oxido nitrates with up to 38 bismuth atoms, e.g., in the nanoscaled $[\text{Bi}_{38}\text{O}_{45}(\text{NO}_3)_{24}]$, using a combined in situ small-angle X-ray scattering (SAXS) and pair distribution function (PDF) analysis approach, as well as electrospray ionization mass spectrometry (ESI-MS) [16–18]. The $\text{Bi}_{38}\text{O}_{45}$ core seems to be the most stable one among the bismuth oxido clusters, and various molecules of this type were reported recently, including sulfonates, salicylates, nitrates, and methacrylates [13,14,19–24]. However, most of them suffer from either low hydrolytic stability at the ligand periphery, low solubility, low biocompatibility of their ligands, or accessibility on a large scale. [18,25]. Previously, we demonstrated that the ligand substitution starting from $[\text{Bi}_{22}\text{O}_{26}(\text{OSiMe}_2^t\text{Bu})_{14}]$ using *tert*-butyloxycarbonyl (Boc)-protected phenylalanine (Phe) (Boc–Phe–OH) gave $[\text{Bi}_{22}\text{O}_{26}(\text{Boc–Phe–O})_{14}]$, which quickly hydrolyses to result in the formation of $[\text{Bi}_{38}\text{O}_{45}(\text{Boc–Phe–O})_{22}(\text{OH})_2]$ [26]. Furthermore, we showed that the substitution of nitrate anions in $[\text{Bi}_{38}\text{O}_{45}(\text{NO}_3)_{20}(\text{dmsO})_{28}](\text{NO}_3)_4 \cdot 4\text{dmsO}$ is possible by the reaction with sodium methacrylate to give $[\text{Bi}_{38}\text{O}_{45}(\text{OMc})_{24}]$ (OMc = Methacrylate), as proven by in situ studies [12,16]. The combined hydrolysis and substitution reaction starting from bismuth nitrate and sodium carboxylates usually tends to give a $[\text{Bi}_{38}\text{O}_{45}]$ cluster core, surrounded by a mixed ligand shell of nitrates and carboxylates [27]. Here, we report the straightforward synthesis of the chiral and highly soluble bismuth oxido cluster $[\text{Bi}_{38}\text{O}_{45}(\text{Boc–Phe–O})_{24}(\text{dmsO})_9]$ by a simple substitution of the nitrate anions in $[\text{Bi}_{38}\text{O}_{45}(\text{NO}_3)_{20}(\text{dmsO})_{28}](\text{NO}_3)_4 \cdot 4\text{dmsO}$ via the reaction with Boc–L–Phe–ONa with a high yield. The solubility of this compound and its functional chiral ligand shell make it attractive for the deposition on diverse substrates. This step is essential for developments in the field of thin films and their applications based on metal oxido clusters, as demonstrated in the rich field of polyoxometalates (POMs), with potential applications ranging from medicine and catalysis [28,29] over energy conversion [30] to electronic [31,32] and electrochromic devices [28]. Reports on deposition methods for neutral metal oxido clusters are so far restricted to rare examples of metal oxido clusters with titanium, tin, hafnium, zirconium, and the lanthanides [33–37].

The deposition of bismuth oxido nanoclusters on surfaces is almost unexplored. We spray-coated $[\text{Bi}_{38}\text{O}_{45}(\text{OMc})_{24}(\text{dmsO})_9]$ on glass surfaces for thin film formation of bismuth(III) oxide after subsequent calcination [38]. Recently, Wu et al. embedded hexanuclear bismuth oxido clusters of the type $[\text{Bi}_6\text{O}_4(\text{OH})_4(\text{NO}_3)_6]$ in a carbon composite material, showing a good capacity for anode materials in lithium-ion batteries [33], while Zhou et al. reported on thin films of similar hexanuclear bismuth oxido/hydroxido nitrates on a glass substrate, covered by a thin aluminium layer. The bismuth oxido clusters showed potential for the use in rewritable resistive memory devices [39]. To the best of our knowledge, the deposition of larger bismuth oxido clusters on a metallic substrate has not yet been reported. Nevertheless, the deposition is a requirement for applications in, e.g., electronic devices or sensors, as reported for other clusters on gold surfaces [40–42].

We report here on the growth mode of the Boc-protected amino acid functionalized chiral bismuth oxido nanocluster $[\text{Bi}_{38}\text{O}_{45}(\text{Boc–L–Phe–O})_{24}(\text{dmsO})_9]$ on Au-coated silicon substrates using spin, drop, and dip coating methods. For the sake of simplicity, we will use the notation $[\text{Bi}_{38}\text{O}_{45}(\text{Boc–Phe–O})_{24}(\text{dmsO})_9]$ throughout the manuscript. The film morphology was analysed using optical microscopy, scanning electron microscopy (SEM), and atomic force microscopy (AFM), in addition to the films characterised using X-ray diffraction (XRD), Fourier transform infrared (FTIR) spectroscopy, and X-ray photoelectron spectroscopy (XPS). We conclude that the Boc–Phe–O modified nanoclusters with $\text{Bi}_{38}\text{O}_{45}$ core were successfully deposited.

2. Materials and Methods

2.1. Materials

N-(*tert*-butoxycarbonyl)-L-phenylalanine (Boc–L–Phe–OH) was purchased from Sigma Aldrich (Steinheim 89555, Germany) and used without further purification. $\text{Bi}(\text{NO}_3)_3 \cdot 5\text{H}_2\text{O}$ was purchased from Alfa Aesar (Kandel 76870, Germany) and used without further purification. $[\text{Bi}_{38}\text{O}_{45}(\text{NO}_3)_{20}(\text{dmsO})_{28}](\text{NO}_3)_4 \cdot 4\text{dmsO}$ (A) was synthesized according to a

literature procedure [13]. Na_2CO_3 (99.5%) from Sigma Aldrich was used without further purification. Acetonitrile purchased from Merck (Darmstadt 64271, Germany) and ethanol (Alfa Aeser) with 99 % purity was used without further purification.

2.2. Synthesis of the Sodium Salt of Boc-Phe-OH (1)

N-(*tert*-butoxycarbonyl)-L-phenylalanine (1.500 g, 5.65 mmol) was dispersed in deionized water (15 mL) under ambient conditions. Na_2CO_3 (300 mg, 2.83 mmol) was added slowly, and gas evolution occurred immediately when the suspension was ultrasonicated for a few seconds ($f = 35$ kHz). The solution was heated to 80°C for 1 h. After filtration and cooling to room temperature, a colourless solid of Boc-L-Phe-ONa (**1**, 1.394 g, 4.85 mmol, 85 %) was obtained after the slow evaporation of the solvent.

^1H NMR (ppm, 500.30 MHz, $\text{dms}\text{-d}_6$, 298 K) $\delta = 7.18$ (m, 5 H), 5.85 (d, 1 H) 3.81 (q, 1 H), 3.05 (dd, 1 H), 2.88 (dd, 1 H), 2.50 (q, $\text{dms}\text{-d}_6$) 1.32 (s, 9 H). ^{13}C NMR (ppm, 125.80 MHz, $\text{dms}\text{-d}_6$, 298 K) 173.9, 154.7, 139.4, 129.7, 127.8, 125.7, 77.4, 56.4, 37.7, 28.4. CHNS (%), expt. and calcd.) for $\text{C}_{14}\text{H}_{18}\text{O}_4\text{NNa}$ ($M = 287.32$ $\text{g}\cdot\text{mol}^{-1}$): C, 58.68 (58.52); H, 6.34 (6.33); N, 4.82 (4.88). IR (cm^{-1}) 3330 m, 3063 w, 3031 w, 2975 m, 2930 w, 1680 m, 1583 s, 1497 m, 1452 w, 1389 s, 1365 s, 1250 m, 1163 s, 1048 m, 1024 m, 852 w, 754 m, 698 s, 561 m, 464 m. (see Figure S1).

2.3. Synthesis of $[\text{Bi}_{38}\text{O}_{45}(\text{Boc-Phe-O})_{24}(\text{dms}\text{-d}_6)_9]$ (2)

The bismuth oxido cluster $[\text{Bi}_{38}\text{O}_{45}(\text{NO}_3)_{20}(\text{dms}\text{-d}_6)_{28}](\text{NO}_3)_4\cdot 4\text{dms}\text{-d}_6$ (**A**, 1.000 g, 0.08 mmol) was dispersed in $\text{dms}\text{-d}_6$ (40 mL) and heated to 80°C for 1 h to give a colourless solution. Boc-L-Phe-ONa (**1**, 837 mg, 2.916 mmol) was added, and the colourless solution was stirred at 80°C for 4 h. The hot solution was filtrated and allowed to cool to room temperature. A colourless solid of **2** was obtained after the slow evaporation of the solvent for a few days. The solid was washed with 15 mL of deionised water and then dried under ambient conditions for two days. Compound **2** was obtained as a colourless solid (1.252 g, 0.08 mmol, 99 % based on bismuth in **A**).

^1H NMR (ppm, 500.30 MHz, $\text{dms}\text{-d}_6$, 298 K) $\delta = 7.15$ (m, 5 H), 6.12 (d, 1 H) 3.91 (q, 1 H), 3.07 (dd, 1 H), 2.84 (dd, 1 H), 2.54 (s, $\text{dms}\text{-d}_6$) 2.50 (q, $\text{dms}\text{-d}_6$) 1.28 (s, 9 H). ^{13}C NMR (ppm, 125.80 MHz, $\text{dms}\text{-d}_6$, 298 K) 173.9, 155.0, 139.2, 129.6, 127.9, 125.9, 77.6, 56.4, 40.4 ($\text{dms}\text{-d}_6$), 37.7, 28.4. CHNS (%), expt. And calcd.) for $\text{Bi}_{38}\text{O}_{150}\text{C}_{354}\text{H}_{486}\text{S}_9\text{N}_{24}$ ($M = 15,708.27$ $\text{g}\cdot\text{mol}^{-1}$): C, 26.60 (27.06); H, 3.19 (3.13); N, 2.82 (2.14); S, 1.81 (1.84). IR (cm^{-1}) 3330 m, 3060 w, 3029 w, 2975 m, 2928 w, 1688 m, 1554 m, 1465 s, 1452 w, 1384 s, 1363 s, 1246 m, 1162 s, 1047 m, 1018 m, 948 w, 854 w, 753 m, 699 s, 528 s. (see Figure S2).

2.4. Film Preparation

The bismuth oxido cluster **2** was dissolved in ethanol as a protic, polar solvent and for comparison in acetonitrile as an aprotic, polar solvent. A concentration of 20 $\text{g}\cdot\text{L}^{-1}$ was applied to all samples. As substrates, 10 mm \times 10 mm pieces of silicon wafers with a 150 nm silicon oxide layer, a 20 nm sputtered titanium layer as an adhesion layer, and 100 nm gold (Au) were used.

Drop coating was performed by covering the substrate with 20 μL of solution and the evaporation of the solvent under ambient conditions.

Spin coating was performed using a Laurell WS-650MZ-23NPPB spin coater (North Wales, USA) with a 4.5 mm vacuum chuck and a pressure of 1 mbar. The coater was operated with a rotation time of 30 s at a rotation speed of 2000 rpm. Moreover, 20 μL of the solution was dropped onto the substrate before the rotation was started.

The dip coating experiments were performed using a SOLGELWAY ACEdip 2.0 dip coater (Sceaux, France). The samples were dipped into 3 mL of the solution at a constant speed of 5 $\text{mm}\cdot\text{s}^{-1}$ for 100 s. Afterwards, the solution was removed with a constant speed of 2 $\text{mm}\cdot\text{s}^{-1}$ and dried under ambient conditions.

The parameters used for the ethanol and acetonitrile samples are shown in Table 1, where the sample name is composed of compound 2, the deposition technique and the solvent, respectively.

Table 1. Deposition parameters for the samples discussed in this work.

Sample Name	Deposition Method	Solvent	Rotation Speed (rpm)	Dip/Withdrawing Speed (mm·s ⁻¹)	Amount of Solution (μL)
2-SpA	spin coating	acetonitrile	2000	-	20
2-SpE	spin coating	ethanol	2000	-	20
2-DiA	dip coating	acetonitrile	-	5/2	-
2-DiE	dip coating	ethanol	-	5/2	-
2-DrA	drop coating	acetonitrile	-	-	20
2-DrE	drop coating	ethanol	-	-	20
2-DrA-2	drop coating	acetonitrile	-	-	50
2-DrE-2	drop coating	ethanol	-	-	50

2.5. Characterization Methods

Optical microscopy imaging was performed with a Nikon IC inspection Microscope ECLIPSE L200 from Nikon Metrology GmbH (Düsseldorf, Germany) with 1× as well as 50× objectives. Atomic force microscopy (AFM) measurements were performed with an atomic force microscope (NanoWorld ArrowTMNCpT AFM, supplied by NanoAndMore GmbH, 35578 Wetzlar, Germany) operating in intermediate topography mode using a *PtIr*₅ cantilever, with resonant frequencies in the range of (240–380) kHz. The analysis of the surface coverage was performed either using Image J (version 2.5.1) [43] (for the optical microscopy images) or Gwyddion software (version 1.52) [44] (for the AFM images).

FTIR spectroscopy was performed in the wavenumber range of (450–5000) cm⁻¹ using a VERTEX 80v FTIR spectrometer with an attenuated total reflectance (ATR) unit from Bruker, Germany. The XPS analysis was performed with an ESCALAB 250Xi photoelectron spectrometer from Thermo Fisher ScientificTM (Waltham, MA, USA) in an ultra-high vacuum (UHV) chamber using a monochromatic Al-K α (1486.68 eV) X-ray source and a beam diameter of 300 μm. The binding energies of all spectra were referenced to the binding energy of C1s (248.8 eV). UV–vis spectra were measured in the diffuse reflection geometry at ambient temperature with an Agilent Technologies Cary 60 UV–vis spectrometer in a range from 200 nm to 800 nm using an optical probe. The data were collected with the *Cary WinUV* Software (version 5.0.0.1005, Santa Clara, CA, USA). Powder X-ray diffractograms were measured at ambient temperature with an STOE *Stadi P* diffractometer (Darmstadt, Germany) using Ge(111)-monochromatized Cu-K α radiation (1.54056 nm, 40 kV, 40 mA). The full width at half maximum (FWHM) is corrected for instrumental broadening using a LaB₆ standard (SRM 660, Gaithersburg, MD, USA) purchased from the National Institute of Standards and Technology (NIST). The value β was corrected using $\beta^2 = \beta_{\text{measured}}^2 - \beta_{\text{instrument}}^2$, where β_{measured} and $\beta_{\text{instrument}}$ are the FWHMs of measured and standard profiles, respectively. Particle size distribution (PSD) based on dynamic light scattering (DLS) was determined using a Zetasizer Nano ZS (Malvern Instruments, Worcestershire, UK, WR14 1XZ), allowing the characterization of suspension in a size range of 0.6 nm to 6 μm. A red laser (633 nm, 4 mW) was used as a light source, and the analyses were performed at an angle of 173° (backscatter NIBS default). The compounds were dissolved in appropriate solvents (20 g·L⁻¹), filtered, filled into glass cuvettes (DTS0012), and measured at 20 °C. Calculation of the PSD was carried out according to the “Mie theory”, assuming the presence of spherical particles. ¹H and ¹³C{¹H} NMR spectra were recorded at room temperature in dmsO-d₆ (dried over 4 Å molecular sieve) with an *Avance III 500* spectrometer (BRUKER, Billerica, MA, USA) at 500.30 MHz and 125.80 MHz, respectively, and were referenced internally to the deuterated solvent relative to Si(CH₃)₄ ($\delta = 0.00$ ppm). Scanning electron microscopy was performed using a NanoNovaSEM200 (Thermo Fisher Scientific, Waltham, MA, USA) device with an electron beam energy of 5 keV and different magnifications.

3. Results and Discussion

3.1. Cluster Synthesis and Characterisation

Starting from $[\text{Bi}_{38}\text{O}_{45}(\text{NO}_3)_{20}(\text{dmsO})_{28}](\text{NO}_3)_4 \cdot 4\text{dmsO}$ (**A**) and the sodium salt of Boc-L-Phe-OH (**1**) in dmsO, $[\text{Bi}_{38}\text{O}_{45}(\text{Boc-Phe-O})_{24}(\text{dmsO})_9]$ (**2**) was obtained after a few days of crystallisation under ambient conditions as a colourless solid with yields > 90%. The elemental analysis confirms the stoichiometry of compound **2**; complete ligand substitution was proven using NMR in combination with IR spectroscopy. The $^1\text{H-NMR}$ spectrum reveals all expected signals for the Boc-Phe-O[−] ligand and is indicative of dmsO coordination to the bismuth oxido cluster in solution (dmsO-d₆), showing a characteristic signal at $\delta = 2.54$ ppm. The IR spectrum shows all expected vibrations of the Boc-protected amino acid-based ligands (Figure S3a). Compared to the sodium salt **1**, the bismuth oxido cluster **2** shows a characteristic broad Bi-O vibration at 580 cm^{-1} [45]. The absence of vibrations at approximately 1740 cm^{-1} ($\nu(\text{N}=\text{O})_{\text{free}}$) for free nitrates, at 1430 cm^{-1} ($\nu_{\text{as.}}(\text{NO}_2)$), 995 cm^{-1} ($\nu_{\text{sym.}}(\text{NO}_2)$) for monodentate, and at 1265 cm^{-1} ($\nu_{\text{sym.}}(\text{NO}_2)$), 1385 cm^{-1} ($\nu_{\text{as.}}(\text{NO}_2)$) for bidentate nitrates, demonstrates the complete exchange of the nitrate ligands (Figure S3b, Table S1) [13,46]. The symmetric valence S=O vibration at 948 cm^{-1} is indicative of dmsO in the resulting compound, which is in line with the NMR results [47]. The presence of Boc-Phe-OH is confirmed by the $\delta_{\text{C-H}}$ vibration of the *tert*-butyl group at 1386 cm^{-1} and 1363 cm^{-1} , the $\delta_{\text{C=C-H}}$ vibration for a monosubstituted aromatic ring at 699 cm^{-1} , 753 cm^{-1} , and 1018 cm^{-1} and the $\nu_{\text{C-N}}$, as well as the $\nu_{\text{C-O}}$ at 1162 cm^{-1} and 1047 cm^{-1} , respectively [45,48,49]. All these vibrations are only slightly shifted compared to Boc-Phe-OH and the sodium salt **1**, however, the symmetric and asymmetric $\nu_{\text{C=O}}$ at 1465 cm^{-1} and 1554 cm^{-1} show significant shifts. In particular, the asymmetric vibration in **2** is shifted to lower wavenumbers by approximately 30 cm^{-1} compared to **1** and by 90 cm^{-1} compared to Boc-Phe-OH, which indicates different coordination to the cluster core.

The preservation of the $[\text{Bi}_{38}\text{O}_{45}]$ cluster core upon the ligand exchange reaction is confirmed using PXRD (Figure S4), which shows a typical diffraction pattern for bismuth oxido nanoclusters, showing one intensive diffraction peak and a much weaker one for $2\theta < 10^\circ$ [18,27]. Compared to the reflections of $[\text{Bi}_{38}\text{O}_{45}(\text{NO}_3)_{20}(\text{dmsO})_{28}](\text{NO}_3)_4 \cdot 4\text{dmsO}$ ($2\theta = 5.23^\circ$ and $2\theta = 6.24^\circ$), the main diffraction peak of **2** is shifted to a lower angle at $2\theta = 4.47^\circ$, indicating an increase in the cluster size of **2** due to the larger ligand shell, compared with the nitrate cluster. The previously reported $[\text{Bi}_{38}\text{O}_{45}(\text{Boc-Phe-OH})_{22}(\text{OH})_2]$ shows similar diffraction peaks, with $2\theta = 4.51^\circ$ and $2\theta = 5.19^\circ$ [26]

The main reflection corresponds to the interlayer distance, assuming a closed, packed nanocluster arrangement [20,50]. Thus, an interlayer distance for **2** of 1.975 nm ($2\theta = 4.47^\circ$) was calculated using Bragg's equation. Compared to the precursor $[\text{Bi}_{38}\text{O}_{45}(\text{NO}_3)_{20}(\text{dmsO})_{28}](\text{NO}_3)_4 \cdot 4\text{dmsO}$ (**A**) with its main reflection at $2\theta = 5.23^\circ$ ($d = 1.688\text{ nm}$), the resulting interlayer distance increases according to the molecule size. In dmsO solution, the mean hydrodynamic diameter was observed in the range of $d_h = (2.2\text{--}2.9)\text{ nm}$ and of $d_h = (1.2\text{--}1.5)\text{ nm}$ for compounds **2** and **A**, respectively. The hydrodynamic diameter was determined from the fitted particle size distribution (PSD) curve based on dynamic light scattering (DLS); the exemplarily results for each solvent are shown in Figure S5. The DLS analysis for the nitrate-substituted bismuth oxido cluster **A** is restricted to the usage of dmsO as a solvent, as a result of its low solubility, whereas cluster **2** is soluble in various organic solvents. Using ethanol as a solvent, the resulting hydrodynamic diameter of **2** is in the range of $d_h = (2.2\text{--}2.9)\text{ nm}$ and of $d_h = (1.4\text{--}1.6)\text{ nm}$, when acetonitrile was used. In the former case, we assume that the bismuth oxido cluster is solvated by the ethanol molecules, providing an increased periphery. In acetonitrile, the partial dissociation of coordinating ligands and solvent, as well as the partial hydrolysis and partial deprotection of the Boc-group, are assumed to give smaller cluster molecules and an asymmetrical molecule shape, which results in a reduced hydrodynamic diameter. Notably, the solubility of **2** is twice as high in ethanol ($\beta = 65\text{ g}\cdot\text{L}^{-1}$) as in acetonitrile ($\beta = 30\text{ g}\cdot\text{L}^{-1}$). However, the cluster core of **2** is stable in both solvents, which makes it suitable for the investigation of solution-based deposition

methods. The influence of solubility as well as of the stabilization and partial dissociation of cluster **2** in solution onto the growth mode of the films on Au is discussed in the following.

In order to test the chemical and structural integrity of compound **2** upon dissolving in various solvents followed by deposition (dip coating, spin coating and drop coating) onto the Au-coated substrates, XRD, ATR-FTIR, and XPS measurements were performed. In the following, the observations made upon dip coating are exemplarily discussed.

The grazing incidence XRD results of the samples deposited by dip coating are shown in Figure 1, and compared to the reference PXRD pattern for **2** measured in the powder diffraction mode. A small shift in the reflections might be expected, considering a slightly different crystal packing in the powder and in the films. The XRD patterns over the full range from $2\theta = 3^\circ$ – 85° are dominated by Au(111), Au(222), Au(311), and Si(400) reflections. For 2-DiE and 2-DiA, only one strong reflection at $2\theta = 4.38^\circ$ and $2\theta = 4.35^\circ$, respectively, is observed, which corresponds to the main reflection peak of **2** at $2\theta = 4.47^\circ$. Thus, we conclude that the deposition of compound **2** was successful.

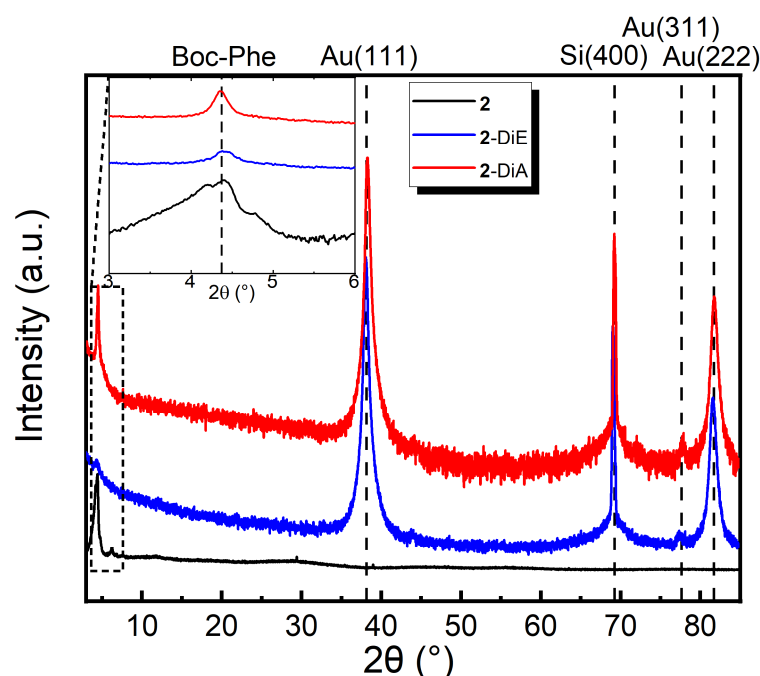


Figure 1. XRD patterns of dip-coated thin films 2-DiE and 2-DiA compared to the PXRD of **2**. The intensity is shown on a logarithmic scale. The inset shows a zoom in the range where the characteristic signature of crystals of **2** is expected.

XPS measurements were carried out to analyse the chemical composition of the films. The survey spectrum (cf. Figure 2a) of a representative sample deposited by dip coating from acetonitrile solution (2-DiA) reveals the typical signals for bismuth (Bi 5d, Bi 5p_{3/2}, Bi 5p_{1/2}, Bi 4f, Bi 4d_{5/2}, Bi 4d_{3/2}, Bi 4p_{3/2}, Bi 4p_{1/2}), oxygen (O 1s) as well as carbon (C 1s) [47,51,52]. A peak at 399.7 eV arising from nitrogen N 1s in the amide groups [53] was observed in the high resolution spectrum (Figure 2b). By contrast, the N 1s peak for the starting material [Bi₃₈O₄₅(NO₃)₂₀(dmsO)₂₈](NO₃)₄·4dmsO (**A**) is observed at 405.8 eV (cf. Figure 2b), which indicates the complete ligand exchange from nitrate to the Boc-protected amino acid carboxylate [46]. In the high resolution spectrum for O 1s, the main peak at 531.4 eV is associated to the C–O bond; the satellite peak at a higher binding energy of 532.9 eV corresponds to the C=O bond (cf. Figure 2c) [54]. The peak at the lower binding energy of 530.1 eV stems from Bi–O bonds in the cluster core [55] (Figure 2c), which proves the existence of the bismuth oxido core after the deposition on the Au-coated substrate. In Figure 2d, the high-resolution spectrum for C 1s is shown. The main peak corresponds to

the sp^3 hybridized carbon of the Boc-protecting group, as well as the CH_3 group in Phe and dmsO.

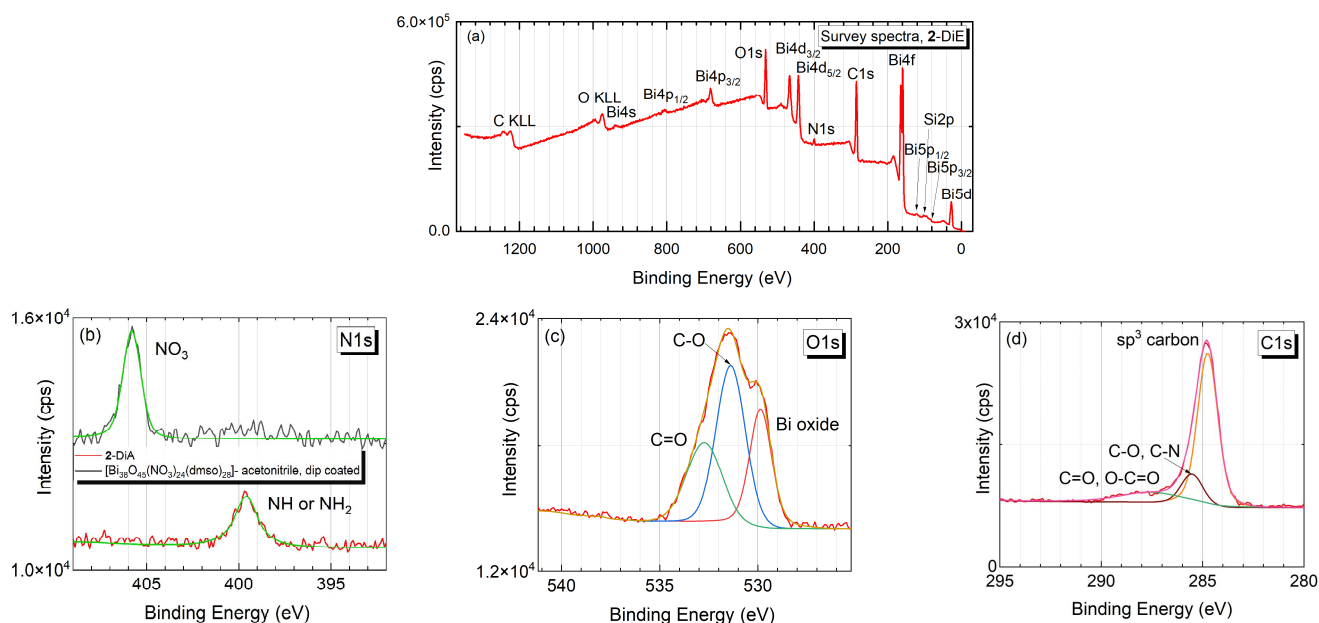
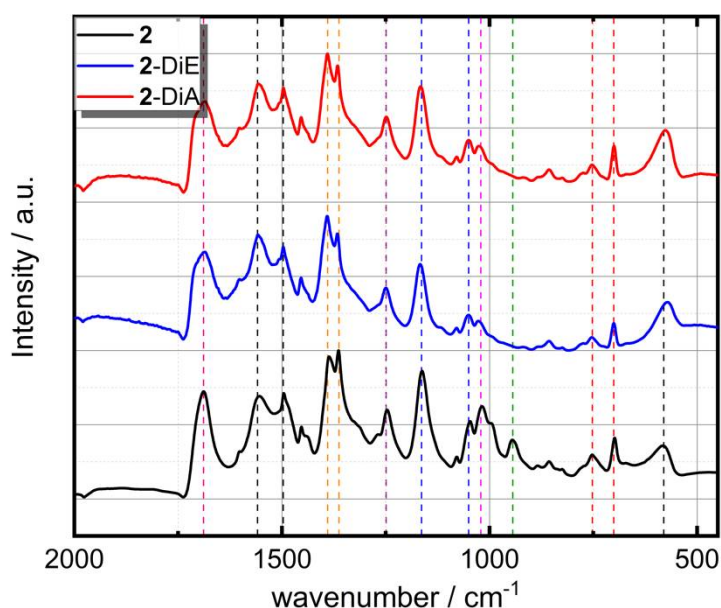


Figure 2. (a) Survey X-ray photoemission spectra of 2-DiA; high resolution spectra for (b) N 1s comparison between 2-DiA and A; a clear indication of successful ligand exchange is provided by the shift to lower binding energies of (c) O 1s and (d) C 1s core levels.

The FTIR spectra of 2-DiA and 2-DiE along with that of **2** are shown exemplarily in Figure 3 and the assigned vibrations are listed in the Table next to it. FTIR data for spin and drop-coated samples are shown in Figure S6 and the assigned vibrations are listed in Table S2.

For all samples, intensive vibrational bands were observed in the range from 570 cm^{-1} – 1700 cm^{-1} . The broad band at approximately 582 cm^{-1} is assigned to the stretching vibration of Bi–O [45], which is slightly broadened and shifted to higher wavenumbers in the films compared to the powder of **2**. In contrast, the bands assigned to the Boc-protected amino acid do not show significant changes. The bands observed at 700 cm^{-1} , 753 cm^{-1} and 1020 cm^{-1} correspond to deformation vibrations of the mono-substituted aromatic system from the Phe unit [45,48]. The intense vibrational modes at 1363 cm^{-1} and 1386 cm^{-1} belong to the symmetric bending mode of C–H (methyl) groups [50]. The bands appearing at 1495 cm^{-1} and 1554 cm^{-1} correspond to the symmetric C=O stretching of carboxylate and at 1688 cm^{-1} to the C=O stretching of amide. The aromatic C–H stretching vibrations above 3000 cm^{-1} and the aliphatic C–H stretching vibration below 3000 cm^{-1} can be assigned to the Boc–Phe–O[−] ligands [50]. The characteristic symmetric S=O vibration band of compound **2** located at approximately 948 cm^{-1} is not present in the films [47]. We conclude that dmsO as solvate of compound **2** is removed upon dissolving in ethanol or acetonitrile, respectively, due to the very low concentration of dmsO in the resulting solutions. This behaviour was recently reported for $[Bi_{38}O_{45}(OMc)_{24}(dmsO)_9] \cdot 2dmsO \cdot 7H_2O$, for which the prior solvate dmsO was displaced by appropriate alcohol solvate molecules according to the solvent used for recrystallization (EtOH or *i*PrOH) [56].

In conclusion, **2** was solubilized in the considered solvents and deposited from solution while retaining the main composition and cluster structure, except for the substitution of coordinating solvent dmsO molecules, whose vibrational signature is not observed in the deposited films. In the following, we discuss the macroscopic growth mode of the clusters on gold surfaces using optical and scanning electron microscopy.



Vibration	2	2-DiE	2-DiA
vBi-O	582	570	576
$\delta_{\text{mono.sub.}}$	699,753	700, 753	100, 752
Aromat			
vS=O	948	917	918
$\delta\text{C-H(C=C-H)}$	1018	1027	1023
vC-N/ vC-O	1047, 1162	1051, 1166	1051, 1163
vC-O-C	1246	1249	1247
$\delta\text{C-H(CH}_3\text{)}$	1363, 1386	1366, 1391	1365, 1389
vC=O Carboxylate	1465, 1554	1496, 1558	1496, 1557
vC=O Amid	1688	1685	1684

Figure 3. FTIR spectra of thin films of 2 deposited by dip coating from acetonitrile (2-DiA) or ethanol (2-DiE) solution and comparison to pure powder of 2, with the associated modes shown in the table at the bottom (values given in cm^{-1}).

3.2. Drop-coated Films

The contact angle of the droplets of the investigated solutions on the Au surface varied from 2° to 8° , which indicates wetting between the Au substrate and all solvents used. According to ref. [57] three main competing flow patterns can occur in droplets of solutions containing colloidal particles when deposited onto a substrate. On one hand, a fast evaporation at the wetting border of the droplet to the unwetted substrate induces a radial flow from the middle of the droplet towards the border, leading to a ring-like agglomeration of the nanoparticles. On the other hand, the presence of a dominant Marangoni recirculating flow would lead to a strong agglomeration of nanoparticles in the middle of

the droplet. Third, the transport of particles towards the substrate driven by Derjaguin–Landau–Verwey–Overbeek (DLVO) interactions may lead either to ring-like patterns or to more homogeneous layers, depending on the pH of the solution.

Depending on the thermophysical properties of the substrate, on the concentration, and on the viscosity as well as on the pH-value of the solution, various structural properties of the films formed by the nanoclusters remaining on the substrate after the solvent evaporation can be achieved. Despite the fact that the phase diagram in ref. [57] was proposed for colloidal nanoparticles with dimensions which are two orders of magnitude larger than those of compound **2**, some similarities between the agglomeration patterns observed in this study and those reported in [57] can be observed.

For a better understanding of the difference in growth behaviour on the edges and the middle of the droplet, SEM images are shown in Figure 4 for 2-DrE films and in Figure 5 for 2-DrA for films deposited from 20 μL solution.

For low viscosity solvents (η) with a high evaporation rate (Γ) like ethanol ($\eta(\text{EtOH}) = 1.2 \text{ mPa}$; $\Gamma(\text{EtOH}) = (0.12 \pm 6.00 \cdot 10^{-3}) \mu\text{L} \cdot \text{s}^{-1} \cdot \text{cm}^{-2}$ and acetonitrile ($\eta(\text{CH}_3\text{CN}) = 0.4 \text{ mPa}$; $\Gamma(\text{CH}_3\text{CN}) = (0.08 \pm 4.10 \cdot 10^{-3}) \mu\text{L} \cdot \text{s}^{-1} \cdot \text{cm}^{-2}$) [58] the turbulences influence the growth behaviour significantly, but the trade-off to pay is the inhomogeneity of the film thickness, which was determined by profilometry. The line profiles obtained for the samples drop-coated from ethanol (2-DrE) and acetonitrile (2-DrA) solution are shown in Figure S7. The maximum height of agglomerations of **2** is observed at the borders of the dried droplet in the case of acetonitrile, while compound **2** is more homogeneously distributed in the case of the deposition from the ethanol solution. The tendency for agglomeration can be understood as a consequence of the stronger intermolecular interaction between the bismuth oxido clusters in solution compared to rather weak interactions between **2** and the gold surface [59].

On the edges of the initial droplets (cf. Figures 4b and 5b) rough agglomerations can be observed. Judging from the form and size of the bismuth oxido cluster agglomerations it can be inferred that in the middle of the droplets (cf. Figures 4c and 5c) the dominant growth mode is the coffee stain effect [57] for both solvents discussed here. Due to the low evaporation rate, agglomerations in the middle of the droplet are observed as well (cf. Figures 4c and 5c).

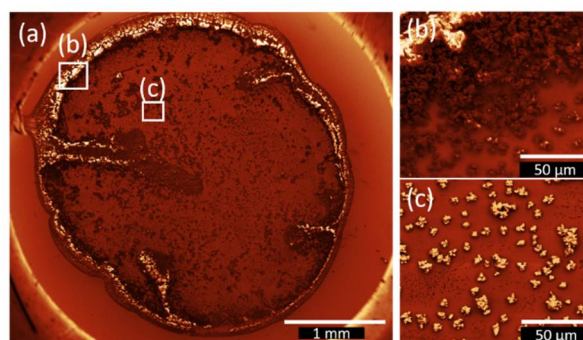


Figure 4. SEM image of 2-DrE film after the evaporation of the solvent. The images were treated with the Gwyddion.net image filter from Gwyddion software: (a) the film shows characteristic features of the coffee stain effect in combination with Ostwald ripening, (b) indicates rough film edges and large agglomerations of bismuth oxido clusters at the drop edge, and (c) displays the middle part of the film with agglomerations of different size next to each other and the trend to more pronounced depletion zones around the larger agglomerations, which is an indicator for Ostwald ripening.

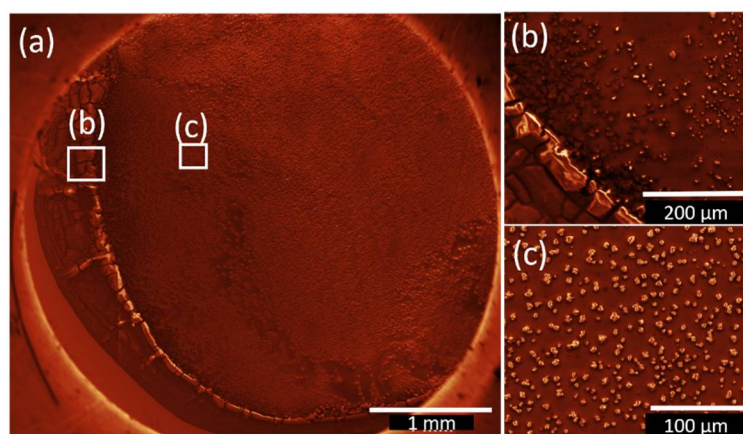


Figure 5. SEM image of 2-DrA film after the evaporation of the solvent. The images were treated with the Gwyddion.net image filter from Gwyddion software: (a) full drop shows the coffee stain effect, (b) indicates rough film edges as well as large cluster agglomerations at the drop edge, and (c) displays the middle part of the droplet with homogeneously distributed agglomerations of similar size.

Furthermore, experiments with higher amount of solution (50 μL), covering the whole substrates were made to determine the difference in growth mode shown in Figures 6 and 7 for ethanol (2-DrE-2) and acetonitrile (2-DrA-2), respectively. As can be seen from the microscopy image in Figure 6a block-like structures separated by cracks are observed on the edge of the substrate which is attributed to the removal of solvent residuals during the drying process, and which may lead to hierarchical crack networks [60]. This phenomenon was also observed for annealed films of bismuth oxide [38]. The volume reduction led to surface tensions and microcracking of the films. Additionally, in Figure 6b–e island growth can be observed. In particular, at the edges of the substrate (Figure 6b), the islands occur as white spots in the SEM images, which is an indicator for charged structures and related to the height. The islands occur as a result of the interaction between several nanoclusters of compound 2.

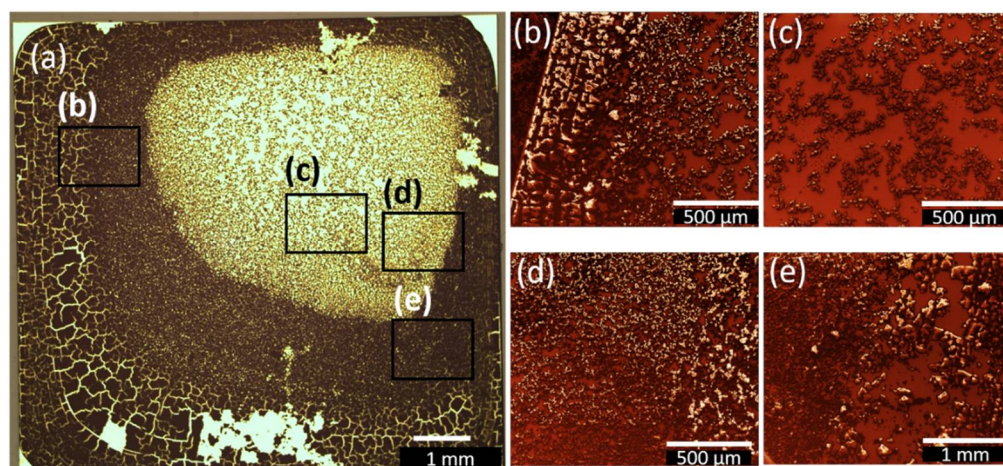


Figure 6. (a) Overview optical microscopy image for 2-DrE-2 after the complete evaporation of ethanol. For better resolution SEM images with the same magnification were chosen in (b–e) at several spots of the sample, shown after applying image filter Gwyddion.net from Gwyddion software. The SEM images indicate island growth behaviour.

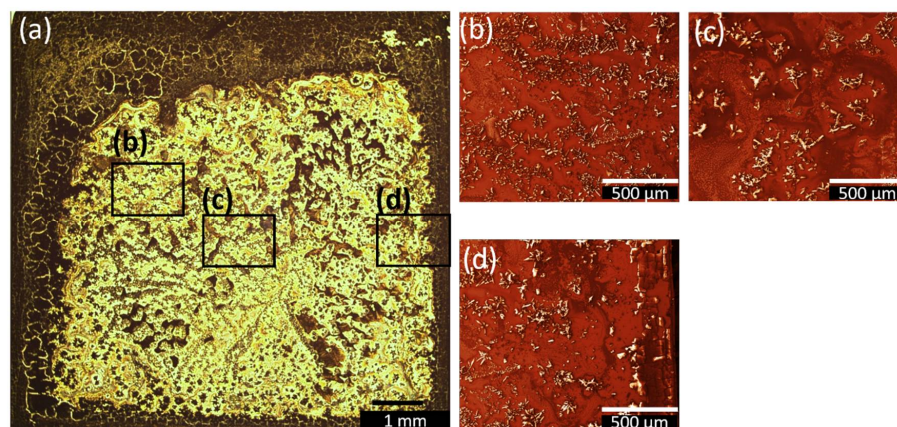


Figure 7. (a) Overview microscopy image for 2-DrA-2 after complete evaporation of acetonitrile. For better resolution, SEM images with same magnification were chosen in (b–d) at several spots of the sample, shown after applying the image filter Gwyddion.net from Gwyddion software. The SEM images indicate areas with dendritic growth typical for diffusion-limited aggregation.

In contrast to the growth behaviour observed for 2-DrE-2 from ethanol solution, the one obtained from acetonitrile is indicating diffusion-limited aggregation in the central droplet region, as presented in Figure 7. Fewer cracks occur on the borders as compared to 2-DrE-2, most likely due to the slightly different evaporation rates of the two solvents. Nevertheless, the dominant growth mode in this sample is diffusion-limited aggregation, since this mechanism is known to lead to the formation of characteristic dendritic, floral structures [61]. Such structures can be reproduced by Monte-Carlo simulations of rate equations for aggregates of atoms, molecules, or ions, and even for defect centres via correlation functions [62], as well as for the wetting of porous media. This occurs when diffusion on the surface is the primary mechanism of mass transport in the system and desorption/adsorption play a minor role [61]. The diffusion leads to the sticking of particles to the nucleation sites at the rim of the aggregates, where the floral-like structure starts growing. The floral-like agglomerations of 2 only occur during the drop and dip coating procedure.

3.3. Spin-coated and Dip-coated Films

In the following, a comparison between the films of the bismuth oxido cluster 2 deposited by spin and dip coating techniques is presented.

Optical microscopy images of spin-coated and dip-coated films from ethanol and acetonitrile solutions are shown in Figure 8 with a magnification of $\times 1$ as well as SEM images for a better resolution with a magnification of $\times 2000$. While the mechanisms discussed in ref. [57] for the formation of nanoparticle agglomerations can be well applied to describe the morphology of the films grown by drop coating (just for 2-DrE and 2-DrA), the images in Figure 8 indicate that films deposited by spin and dip coating are not subjected to severe concentration gradients during growth.

In the case of spin- and dip-coated samples the coffee stain effect was not observed. Compared to the case of drop coating, a tendency of agglomeration of compound 2 is observable, with the main difference that in the case of spin and dip-coated samples homogeneously distributed agglomerations over the whole substrate are observed (for dip coating—over the whole dipped area). The homogeneous distribution of the agglomerations can be related to the faster spreading of the solution; hence the droplet size is reduced in the case of spin and dip coating. This, in turn, reduces the contribution of the radial flow towards the droplet edge, and hence the radial concentration gradients.

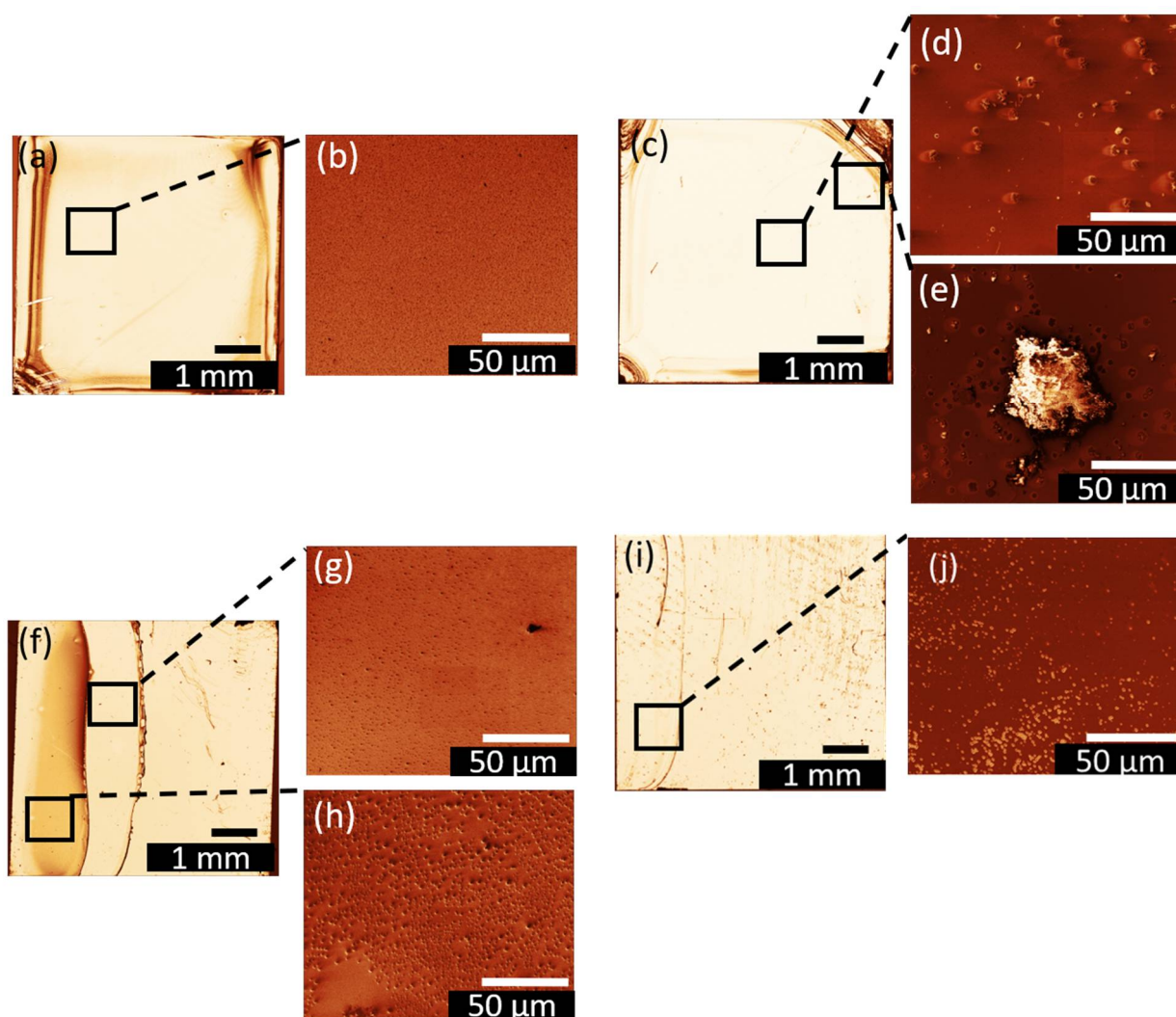


Figure 8. Light microscopy images with insets from SEM images of spin- and dip-coated films treated with the Gwyddion.net image filter from Gwyddion software for (a), (b) 2-SpE, (c–e) 2-SpA, (f–h) 2-DiE and (i), (k) 2-DiA.

The area covered by the single aggregates is larger in the case of acetonitrile than for ethanol solution (see Figure 8b,d, respectively). The larger size of agglomerations grown from acetonitrile solution is consistent with the fact that the solubility in ethanol is more than twice as high as for acetonitrile. As the two solutions are equimolar, precipitation of 2 will start earlier from acetonitrile and the aggregates have more time to grow and coagulate. This effect is enhanced by the lower evaporation rate of acetonitrile compared to ethanol. Notably, the solubility experiments proved that the resulting agglomerates of 2 dissolved in ethanol are smaller due to the better solubility. Next to the island formation, Ostwald ripening [61] was observed, especially for 2-SpA (cf. Figure 8e). This phenomenon occurs in a liquid environment and leads to bigger agglomerates separated by an empty zone from the smaller ones, which get dissolved during the growth process of the larger ones. Ostwald ripening is a thermodynamically driven process, which minimizes the island edge line, and the high surface to volume ratio is decreased by the formation of big agglomerates. By comparing the particle area of the two samples obtained from ethanol and acetonitrile, the difference between the two solvents used is quite obvious, and the calculated particle density for acetonitrile samples is much lower than that of ethanol ones (cf. Table 2). The highest possible coverage of $(59.95 \pm 3.00)\%$ was achieved for the 2-SpE sample. Overall, full coverage of the substrate by 2 cannot be achieved with the

chosen deposition parameters. The coverage extracted from all microscopy images shown in Figure 8 are presented in Table 2.

AFM measurements were performed to determine the height and the shape of the agglomerations. Micrometer-sized 3D aggregate shapes are obtained in all cases. The results are shown in Figure 9 and the associated maximum heights are summarized in Table 2. The floral structure grown during dip coating from ethanol solution (Figure 9c) shows flatter maximum height than the smaller islands formed (cf. Figure 9a,b,d). The origin of the island height difference observed for the two deposition methods is not fully understood. The fractal boundary shape again suggests further growth on the gold surface by diffusion-limited aggregation. In both cases indications for Ostwald ripening of larger particles at the expense of smaller ones are present. Depending on the solvent evaporation rate one or the other mechanism dominates, as discussed in more detail below.

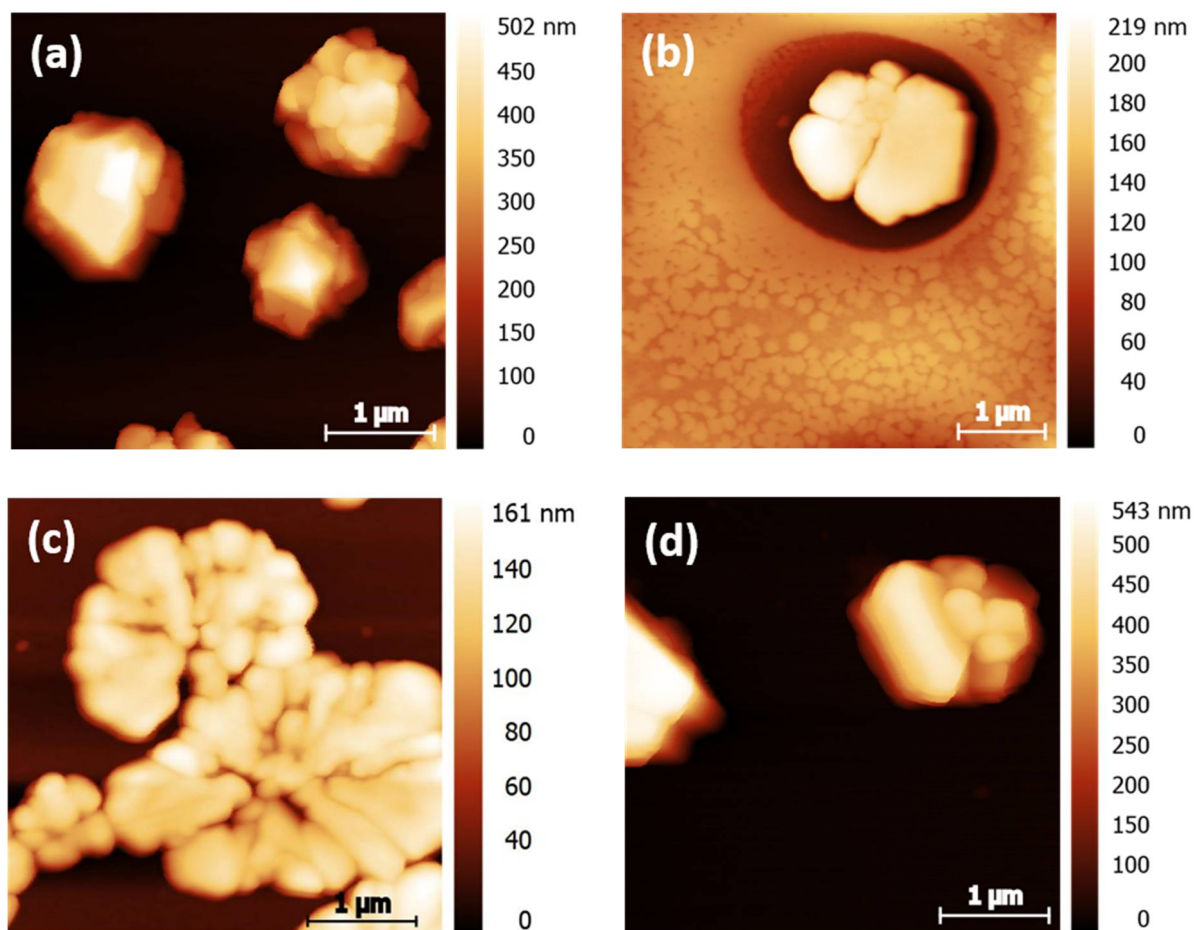


Figure 9. AFM images of (a) 2-SpE, (b) 2-SpA, (c) 2-DiE, and (d) 2-DiA films. In (a,b,d) islands of sub- μm lateral size and heights are visible. Their density depends on the choice of the solvent and on the deposition method. In the case of dip coating in ethanol solution (c), a floral pattern is formed.

For the spin-coated samples shown in Figure 9a,b islands with well-defined terraces are formed. For the ethanol spin-coated sample shown in Figure 9 a combination of large and small islands can be observed. Interestingly, in the vicinity of large particles, a large area is depleted from islands; this dark red area of the image probably corresponds to pure Au. A “void” depletion region surrounding the cluster, which is typical for Ostwald ripening, can also be seen in the microscopy image of samples spin-coated from acetonitrile in Figure 9b as a light white shadow of the agglomerates. In some cases, those shadows, corresponding to the gold surface, are elliptically shaped with the long axis of the ellipse pointing in the same direction. It is well possible that this characteristic shape is a result of

the outward flow of the solution, fast evaporation time during the spinning process and the lower solubility of compound **2** in acetonitrile.

The dominant growth mode in the sample shown in Figure 9c is the diffusion-limited aggregation [61]. The floral-like agglomerations of **2** only occurs during the drop (see above, different scales) and dip coating procedure. Therefore, it can be assumed that this aggregates shape is related to the available time for the formation of this floral pattern. If the solvent is not fully evaporated during the retraction of the substrate, the nanoclusters of **2** have sufficient time to agglomerate.

Table 2. Particle densities of the films extracted from the optical microscopy images shown in Figure 8 and maximum height for agglomerations extracted from the AFM images shown in Figure 9.

Sample	Particle Density/% (Microscopy Images)	Maximum Island Height/nm (AFM)
2-SpE	(60.0 ± 3.0)	(502 ± 25)
2-SpA	(4.1 ± 0.4)	(219 ± 11)
2-DiE	(28.6 ± 1.4)	(161 ± 8)
2-DiA	(13.8 ± 0.2)	(543 ± 27)

Summarizing, the deposition of bismuth oxido cluster **2** from different solutions and using three different deposition methods can lead to the formation of agglomerations or islands of different shape and size. Considering the XRD results, these structures are crystalline (see Figures S8 and S9).

4. Conclusions

In this work, the high-yield conversion of the bismuth subnitrate $[\text{Bi}_{38}\text{O}_{45}(\text{NO}_3)_{20}(\text{dmsO})_{28}](\text{NO}_3)_4 \cdot 4\text{dmsO}$ into the chiral bismuth oxido nanocluster $[\text{Bi}_{38}\text{O}_{45}(\text{Boc-Phe-O})_{24}(\text{dmsO})_9]$ (**2**) is demonstrated. The nanocluster **2** shows a hydrodynamic diameter of (1.4–1.6) nm (in CH_3CN) and (2.2–2.9) nm (in Ethanol) according to DLS. PXRD results are in line with a diameter of approximately 2 nm. Cluster **2** is soluble in a variety of organic solvents, which makes deposition methods from solution such as spin, dip and drop coating attractive. Using XRD, XPS and FTIR spectroscopy, it is demonstrated that the cluster core stays intact upon deposition on gold surfaces. Macroscopically, the films obtained by drop coating are neither homogeneous nor do they spread over a large area by using the same amount of solution compared to spin and dip coating. Optical microscopy as well as SEM images show that the growth behaviour in drop coating can be explained by the coffee ring effect. By the usage of more solution, cracked, very rough structures with a tendency to diffusion-limited aggregation were observed. By using spin and dip coating methods, bismuth oxido cluster agglomerations with a lateral size on the micrometre scale were obtained. The lateral dimensions of the crystalline agglomerates are nearly monodisperse and the distance between the neighbouring micro-agglomerates is nearly constant. Since their size can be controlled by the choice of solvent and of the deposition method, compound **2** could be suitable for the growth of high-density bismuth oxido micro or nanostructures on prepatterned surfaces, where the pre patterning provides nucleation centres. Finally, this study provides a basis for further studies on wafer scale deposition of micro and nanostructures made of neutral metal oxido nanoclusters on metal surfaces, that are promising heterostructures for electronic or photonic applications.

Supplementary Materials: The following supporting information can be downloaded at: <https://www.mdpi.com/article/10.3390/nano12111815/s1>, Figure S1. (a) ^1H NMR spectra (500.3 MHz, 298 K) of **1** in dmsO-d_6 . (b) ^{13}C NMR spectra (125.8 MHz, 298 K) of **1** in dmsO-d_6 ; Figure S2. (a) ^1H NMR spectra (500.3 MHz, 298 K) of **2** in dmsO-d_6 . (b) ^{13}C NMR spectra (125.8 MHz, 298 K) of **2** in dmsO-d_6 ; Figure S3. (a) FTIR spectra of Boc-Phe sodium salt (**1**, violet) and $[\text{Bi}_{38}\text{O}_{45}(\text{Boc-Phe-O})_{24}(\text{dmsO})_9]$ (**2**, black) powder, (b) FTIR spectra of $[\text{Bi}_{38}\text{O}_{45}(\text{NO}_3)_{20}(\text{dmsO})_{28}](\text{NO}_3)_4 \cdot 4\text{dmsO}$ (**A**, green) and $[\text{Bi}_{38}\text{O}_{45}(\text{Boc-Phe-O})_{24}(\text{dmsO})_9]$ (**2**, black) powder; Table S1. FTIR vibration modes

of $[\text{Bi}_{38}\text{O}_{45}(\text{NO}_3)_{20}(\text{dmsO})_{28}](\text{NO}_3)_4 \cdot 4\text{dmsO}$ **A** associated with the FTIR spectrum in Figure S1(b); Figure S4. PXRD pattern of $[\text{Bi}_{38}\text{O}_{45}(\text{NO}_3)_{20}(\text{dmsO})_{28}](\text{NO}_3)_4 \cdot 4\text{dmsO}$ (**A**, green) and $[\text{Bi}_{38}\text{O}_{45}(\text{Boc-Phe-O})_{24}(\text{dmsO})_9]$ powder (**2**, black); Figure S5. Exemplary particle size distribution (PSD) of $[\text{Bi}_{38}\text{O}_{45}(\text{NO}_3)_{20}(\text{dmsO})_{28}](\text{NO}_3)_4 \cdot 4\text{dmsO}$ (**A**), (**a**) and **2** in dmsO (**b**), in acetonitrile (**c**) and in ethanol (**d**). The data for PSD curve of **A** were used with permission from ref [63]; Table S2. FTIR vibration modes of **2** associated with FTIR spectrum in Figure 1 and Figure S4 (**a**) **2**, (**b**) **2-DrA**, (**c**) **2-DrE**, (**d**) **2-SpA** and (**e**) **2-SpE** (**f**) **2-DrA-2** (**g**) **2-DrE-2** (values given in cm^{-1}); Figure S6. FTIR spectra for drop and spin coated films, **2** dissolved in ethanol (DrE and SpE) and acetonitrile (DrA and SpA) and double coated films from **2** dissolved in ethanol and acetonitrile for drop coated samples (**2-DrE-2** and **2-DrA-2**); Figure S7. Profilometry of deposited films from bismuth oxido cluster **2** dissolved in ethanol (DrE) and in acetonitrile (DrA), respectively; Figure S8. Comparison of XRD of compound **2** and drop coated films of **2** from ethanol (**2-DrE**) and acetonitrile (**2-DrA**) solution; Figure S9. Comparison of XRD of compound **2**, spin coated samples of **2** from ethanol 5 μL and 1000 rpm, ethanol with 20 μL and 2000 rpm (**2-SpE**), and from acetonitrile 20 μL and 2000 rpm (**2-SpA**) solution.

Author Contributions: Conceptualization, A.M., R.T., G.S. and M.M.; methodology, A.M., R.T.; validation, A.S., S.G., D.R.T.Z.; formal analysis, A.M., R.T., O.S., C.T. and S.G.; investigation, A.M., R.T., O.S., I.M., M.W., A.S. and D.D.; visualization, A.M., R.T.; writing—original draft preparation, A.M. and R.T.; writing—review and editing, all authors; supervision, G.S., M.M., C.T. and D.R.T.Z. All authors have read and agreed to the published version of the manuscript.

Funding: A.S. and G.S. would like to acknowledge financial support from DFG project no. 282193534. The publication of this article was funded by Chemnitz University of Technology and by the Deutsche Forschungsgemeinschaft (DFG, German Research Foundation)—491193532. SG acknowledges support by the Deutsche Forschungsgemeinschaft via project INST 270/290-1 FUGB.

Data Availability Statement: The data presented in this study are available in this article and in the Supplementary Material.

Acknowledgments: We thank Jana Buschmann for CHNS analyses. We would like to thank Maria Almeida-Hofmann and Stefan Schulz for the possibility to use the light microscope. S.G. thanks Thomas Gemming for valuable discussions.

Conflicts of Interest: The authors declare no conflict of interest. The funders had no role in the design of the study; in the collection, analyses, or interpretation of data; in the writing of the manuscript, or in the decision to publish the results.

References

1. Qin, K.; Zhao, Q.; Yu, H.; Xia, X.; Li, J.; He, S.; Wei, L.; An, T. A review of bismuth-based photocatalysts for antibiotic degradation: Insight into the photocatalytic degradation performance, pathways and relevant mechanisms. *Environ. Res.* **2021**, *199*, 111360. [[CrossRef](#)] [[PubMed](#)]
2. Ereemeev, S.V.; Koroteev, Y.M.; Chulkov, E.V. Surface electronic structure of bismuth oxychalcogenides. *Phys. Rev. B* **2019**, *100*, 115417. [[CrossRef](#)]
3. Ferhat, M.; Zaoui, A. Structural and electronic properties of III-V bismuth compounds. *Phys. Rev. B* **2006**, *73*, 115107. [[CrossRef](#)]
4. Bartoli, M.; Jagdale, P.; Tagliaferro, A. A Short Review on Biomedical Applications of Nanostructured Bismuth Oxide and Related Nanomaterials. *Materials* **2020**, *13*, 5234. [[CrossRef](#)]
5. Lichtenberg, C. Molecular bismuth(III) monocations: Structure, bonding, reactivity, and catalysis. *Chem. Comm.* **2021**, *57*, 4483–4495. [[CrossRef](#)]
6. Magre, M.; Kuziola, J.; Nöthling, N.; Cornella, J. Dibismuthanes in catalysis: From synthesis and characterization to redox behavior towards oxidative cleavage of 1,2-diols. *Org. Biomol. Chem.* **2021**, *19*, 4922–4929. [[CrossRef](#)]
7. Levent, E.; Sala, O.; Wilm, L.F.B.; Löwe, P.; Dielmann, F. Heterobimetallic complexes composed of bismuth and lithium carboxylates as polyurethane catalysts—Alternatives to organotin compounds. *Green Chem.* **2021**, *23*, 2747–2755. [[CrossRef](#)]
8. Potenti, S.; Gualandi, A.; Puggioli, A.; Fermi, A.; Bergamini, G.; Cozzi, P.G. Photoredox Allylation Reactions Mediated by Bismuth in Aqueous Conditions. *Eur JOC* **2021**, *2021*, 1624–1627. [[CrossRef](#)]
9. Moon, H.W.; Cornella, J. Bismuth Redox Catalysis: An Emerging Main-Group Platform for Organic Synthesis. *ACS Catal.* **2022**, *12*, 1382–1393. [[CrossRef](#)]
10. Ochiai, B.; Kikuta, K.; Matsumura, Y.; Horikoshi, H.; Furukawa, K.; Miyamoto, M.; Nishimura, Y. Transparent and Photochromic Material Prepared by Copolymerization of Bismuth(III) Methacrylate. *ACS Appl. Poly. Mater.* **2021**, *3*, 4419–4423. [[CrossRef](#)]

11. Arnold, J.; Sarkar, K.; Smith, D. 3D printed bismuth oxide-polylactic acid composites for radio-mimetic computed tomography spine phantoms. *J. Biomed. Mater. Res. B Appl. Biomater.* **2021**, *109*, 789–796. [[CrossRef](#)] [[PubMed](#)]
12. Negussie, A.H.; de Ruiter, Q.M.B.; Britton, H.; Donahue, D.R.; Boffi, Q.; Kim, Y.-S.; Pritchard, W.F.; Moonen, C.; Storm, G.; Lewis, A.L.; et al. Synthesis, characterization, and imaging of radiopaque bismuth beads for image-guided transarterial embolization. *Sci. Rep.* **2021**, *11*, 533. [[CrossRef](#)] [[PubMed](#)]
13. Miersch, L.; Schlesinger, M.; Troff, R.W.; Schalley, C.A.; Ruffer, T.; Lang, H.; Zahn, D.; Mehring, M. Hydrolysis of a Basic Bismuth Nitrate-Formation and Stability of Novel Bismuth Oxido Clusters. *Chem. Eur. J.* **2011**, *17*, 6985–6990. [[CrossRef](#)]
14. Miersch, L.; Ruffer, T.; Schlesinger, M.; Lang, H.; Mehring, M. Hydrolysis studies on bismuth nitrate: Synthesis and crystallization of four novel polynuclear basic bismuth nitrates. *Inorg. Chem.* **2012**, *51*, 9376–9384. [[CrossRef](#)] [[PubMed](#)]
15. Udalova, T.A.; Logutenko, O.A.; Timakova, E.V.; Afonina, L.I.; Naydenko, E.S.; Yukhin, Y.M. Bismuth compounds in medicine. In Proceedings of the Third International Forum on Strategic Technologies, Novosibirsk, Russia, 23–29 June 2008; pp. 137–140.
16. Anker, A.S.; Christiansen, T.L.; Weber, M.; Schmiele, M.; Brok, E.; Kjær, E.T.S.; Juhás, P.; Thomas, R.; Mehring, M.; Jensen, K.M.Ø. Structural Changes during the Growth of Atomically Precise Metal Oxido Nanoclusters from Combined Pair Distribution Function and Small-Angle X-ray Scattering Analysis. *Angew. Chem. Int. Ed.* **2021**, *60*, 20407–20416. [[CrossRef](#)]
17. Sattler, D.; Schlesinger, M.; Mehring, M.; Schalley, C.A. Mass Spectrometry and Gas-Phase Chemistry of Bismuth–Oxido Clusters. *ChemPlusChem* **2013**, *78*, 1005–1014. [[CrossRef](#)]
18. Weber, M.; Schlesinger, M.; Walther, M.; Zahn, D.; Schalley, C.A.; Mehring, M. Investigations on the growth of bismuth oxido clusters and the nucleation to give metastable bismuth oxide modifications. *Z. Kristallogr.—Cryst. Mater.* **2017**, *232*, 185–207. [[CrossRef](#)]
19. Szczerba, D.; Tan, D.; Do, J.-L.; Titi, H.M.; Mouhtadi, S.; Chaumont, D.; del Carmen Marco de Lucas, M.; Geoffroy, N.; Meyer, M.; Rousselin, Y.; et al. Real-Time Observation of “Soft” Magic-Size Clusters during Hydrolysis of the Model Metallodrug Bismuth Disalicylate. *JACS* **2021**, *143*, 16332–16336. [[CrossRef](#)]
20. Wrobel, L.; Ruffer, T.; Korb, M.; Krautscheid, H.; Meyer, J.; Andrews, P.C.; Lang, H.; Mehring, M. Homo- and Heteroleptic Coordination Polymers and Oxido Clusters of Bismuth(III) Vinylsulfonates. *Chem. Eur. J.* **2018**, *24*, 16630–16644. [[CrossRef](#)]
21. Miersch, L.; Ruffer, T.; Mehring, M. Organic–inorganic hybrid materials starting from the novel nanoscaled bismuth oxido methacrylate cluster $[\text{Bi}_{38}\text{O}_{45}(\text{OMe})_{24}(\text{DMSO})_9] \cdot 2\text{DMSO} \cdot 7\text{H}_2\text{O}$. *Chem. Comm.* **2011**, *47*, 6353–6355. [[CrossRef](#)]
22. André, V.; Hardeman, A.; Halasz, I.; Stein, R.S.; Jackson, G.J.; Reid, D.G.; Duer, M.J.; Curfs, C.; Duarte, M.T.; Frišćić, T. Mechanosynthesis of the metallodrug bismuth subsalicylate from Bi_2O_3 and structure of bismuth salicylate without auxiliary organic ligands. *Angew. Chem.* **2011**, *123*, 8004–8007. [[CrossRef](#)]
23. Andrews, P.C.; Deacon, G.B.; Forsyth, C.M.; Junk, P.C.; Kumar, I.; Maguire, M. Towards a structural understanding of the anti-ulcer and anti-gastritis drug bismuth subsalicylate. *Angew. Chem.* **2006**, *118*, 5766–5770. [[CrossRef](#)]
24. Ding, Q.-R.; Yu, Y.; Cao, C.; Zhang, J.; Zhang, L. Stepwise assembly and reversible structural transformation of ligated titanium coated bismuth-oxo cores: Shell morphology engineering for enhanced chemical fixation of CO_2 . *Chem. Sci.* **2022**, *13*, 3395–3401. [[CrossRef](#)] [[PubMed](#)]
25. Mehring, M. From Molecules to Bismuth Oxide-Based Materials: Potential Homo- and Heterometallic Precursors and Model Compounds. *Coord. Chem. Rev.* **2007**, *251*, 974. [[CrossRef](#)]
26. Mansfeld, D.; Miersch, L.; Ruffer, T.; Schaarschmidt, D.; Lang, H.; Böhle, T.; Troff, R.W.; Schalley, C.A.; Müller, J.; Mehring, M. From $\{\text{Bi}_{22}\text{O}_{26}\}$ to Chiral Ligand-Protected $\{\text{Bi}_{38}\text{O}_{45}\}$ -Based Bismuth Oxido Clusters. *Chem. Eur. J.* **2011**, *17*, 14805–14810. [[CrossRef](#)]
27. Schlesinger, M.; Weber, M.; Ruffer, T.; Lang, H.; Mehring, M. Nanoscaled Bismuth Oxido Clusters: Probing Factors of Structure Formation and Photocatalytic Activity. *EurJIC* **2014**, *2014*, 302–309. [[CrossRef](#)]
28. Wang, S.-M.; Hwang, J.; Kim, E. Polyoxometalates as promising materials for electrochromic devices. *J. Mat. Chem. C* **2019**, *7*, 7828–7850. [[CrossRef](#)]
29. Cherevan, A.S.; Nandan, S.P.; Roger, I.; Liu, R.; Streb, C.; Eder, D. Polyoxometalates on Functional Substrates: Concepts, Synergies, and Future Perspectives. *Adv. Sci.* **2020**, *7*, 1903511. [[CrossRef](#)]
30. Ji, Y.; Huang, L.; Hu, J.; Streb, C.; Song, Y.-F. Polyoxometalate-functionalized nanocarbon materials for energy conversion, energy storage and sensor systems. *Energy Environ. Sci.* **2015**, *8*, 776–789. [[CrossRef](#)]
31. Busche, C.; Vilà-Nadal, L.; Yan, J.; Miras, H.N.; Long, D.-L.; Georgiev, V.P.; Asenov, A.; Pedersen, R.H.; Gadegaard, N.; Mirza, M.M.; et al. Design and fabrication of memory devices based on nanoscale polyoxometalate clusters. *Nature* **2014**, *515*, 545–549. [[CrossRef](#)]
32. Dianat, S.; Hatefi-Mehrjardi, A.; Mahmoodzadeh, K. Electrochemical behavior of inorganic–organic hybrid polyoxometalate ((Cys) $_3$ [PW $_{12}$ O $_{40}$]) nanostructure self-assembled monolayer on polycrystalline gold electrode surfaces. *New J. Chem.* **2019**, *43*, 1388–1397. [[CrossRef](#)]
33. Wu, K.; Shao, L.; Jiang, X.; Shui, M.; Ma, R.; Lao, M.; Lin, X.; Wang, D.; Long, N.; Ren, Y.; et al. Facile preparation of $[\text{Bi}_6\text{O}_4](\text{OH})_4(\text{NO}_3)_6 \cdot 4\text{H}_2\text{O}$, $[\text{Bi}_6\text{O}_4](\text{OH})_4(\text{NO}_3)_6 \cdot \text{H}_2\text{O}$ and $[\text{Bi}_6\text{O}_4](\text{OH})_4(\text{NO}_3)_6 \cdot \text{H}_2\text{O}/\text{C}$ as novel high capacity anode materials for rechargeable lithium-ion batteries. *J. Power Source* **2014**, *254*, 88–97. [[CrossRef](#)]
34. Stehlin, F.; Wieder, F.; Spangenberg, A.; Le Meins, J.-M.; Soppera, O. Room-temperature preparation of metal-oxide nanostructures by DUV lithography from metal-oxo clusters. *J. Mat. Chem. C* **2014**, *2*, 277–285. [[CrossRef](#)]

35. Cardineau, B.; Del Re, R.; Marnell, M.; Al-Mashat, H.; Vockenhuber, M.; Ekinci, Y.; Sarma, C.; Freedman, D.A.; Brainard, R.L. Photolithographic properties of tin-oxo clusters using extreme ultraviolet light (13.5nm). *Microelectron. Eng.* **2014**, *127*, 44–50. [[CrossRef](#)]
36. Marsh, D.A.; Goberna-Ferrón, S.; Baumeister, M.K.; Zakharov, L.N.; Nyman, M.; Johnson, D.W. Ln polyoxocations: Yttrium oxide solution speciation & solution deposited thin films. *Dalton Trans.* **2017**, *46*, 947–955.
37. Gross, S. Oxocluster-reinforced organic–inorganic hybrid materials: Effect of transition metal oxoclusters on structural and functional properties. *J. Mat. Chem.* **2011**, *21*, 15853–15861. [[CrossRef](#)]
38. Hofmann, M.; Rößner, L.; Armbrüster, M.; Mehring, M. Thin Coatings of α - and β -Bi₂O₃ by Ultrasonic Spray Coating of a Molecular Bismuth Oxido Cluster and their Application for Photocatalytic Water Purification Under Visible Light. *ChemistryOpen* **2020**, *9*, 277–284. [[CrossRef](#)]
39. Zhou, K.; Ding, G.; Zhang, C.; Lv, Z.; Luo, S.; Zhou, Y.; Zhou, L.; Chen, X.; Li, H.; Han, S.-T. A solution processed metal–oxo cluster for rewritable resistive memory devices. *J. Mater. Chem. C* **2019**, *7*, 843–852. [[CrossRef](#)]
40. Ford, M.J.; Masens, C.; Cortie, M.B. The application of gold surface and particles in nanotechnology. *Surf. Rev. Lett.* **2006**, *13*, 297–307. [[CrossRef](#)]
41. Fendler, J.H. Chemical Self-assembly for Electronic Applications. *Chem. Mat.* **2001**, *13*, 3196–3210. [[CrossRef](#)]
42. Newton, L.; Slater, T.; Clark, N.; Vijayaraghavan, A. Self assembled monolayers (SAMs) on metallic surfaces (gold and graphene) for electronic applications. *J. Mat. Chem. C* **2013**, *1*, 376–393. [[CrossRef](#)]
43. Collins, T.J. ImageJ for microscopy. *BioTechniques* **2007**, *43*, S25–S30. [[CrossRef](#)]
44. Nečas, D.; Klapetek, P. Gwyddion: An open-source software for SPM data analysis. *Cent. Eur. J. Phys.* **2012**, *10*, 181–188. [[CrossRef](#)]
45. Nakamoto, K. Infrared and Raman Spectra of Inorganic and Coordination Compounds. In *Handbook of Vibrational Spectroscopy*; John Wiley & Sons: Hoboken, NJ, USA, 2006.
46. Weber, M.; Ruffer, T.; Speck, F.; Göhler, F.; Weimann, D.P.; Schalley, C.A.; Seyller, T.; Lang, H.; Mehring, M. From a Cerium-Doped Polynuclear Bismuth Oxido Cluster to β -Bi₂O₃:Ce. *Inorg. Chem.* **2020**, *59*, 3353–3366. [[CrossRef](#)] [[PubMed](#)]
47. Cotton, F.A.; Francis, R.; Horrocks, W.D. Sulfoxides as ligands. II. The infrared spectra of some dimethyl sulfoxide complexes. *J. Phys. Chem.* **1960**, *64*, 1534–1536. [[CrossRef](#)]
48. Socrates, G. *Infrared and Raman Characteristic Group Frequencies: Tables and Charts*; John Wiley & Sons: Hoboken, NJ, USA, 2004.
49. Coates, J. Interpretation of Infrared Spectra, A Practical Approach. In *Encyclopedia of Analytical Chemistry*; John Wiley & Sons: Hoboken, NJ, USA, 2006.
50. Wrobel, L.; Ruffer, T.; Korb, M.; Lang, H.; Mehring, M. Bismuth(III) Anthranilates—Synthesis and Characterization of a Coordination Polymer and a Polynuclear Oxido Cluster. *Eur JIC* **2017**, *2017*, 1032–1040. [[CrossRef](#)]
51. Nohira, H.; Tsai, W.; Besling, W.; Young, E.; Petry, J.; Conard, T.; Vandervorst, W.; De Gendt, S.; Heyns, M.; Maes, J.; et al. Characterization of ALCVD-Al₂O₃ and ZrO₂ layer using X-ray photoelectron spectroscopy. *J. Non. Cryst. Solids.* **2002**, *303*, 83–87. [[CrossRef](#)]
52. NIST. *NIST X-ray Photoelectron Spectroscopy Database*; Volume NIST Standard Reference Database Number 20; National Institute of Standards and Technology: Gaithersburg, MD, USA, 2000; p. 20899.
53. Rignanesi, G.M.; Pasquarello, A.; Charlier, J.C.; Gonze, X.; Car, R. Nitrogen Incorporation at Si(100) -SiO₂ Interfaces: Relation between N1s Core-Level Shifts and Microscopic Structure. *Phys. Rev. Lett.* **1997**, *79*, 5174–5177. [[CrossRef](#)]
54. Shchukarev, A.V.; Korolkov, D.V. XPS Study of group IA carbonates. *Cent. Eur. J. Chem.* **2004**, *2*, 347–362. [[CrossRef](#)]
55. Uchida, K.; Ayame, A. Dynamic XPS measurements on bismuth molybdate surfaces. *Surf. Sci.* **1996**, *357*–*358*, 170–175. [[CrossRef](#)]
56. Weber, M.; Thiele, G.; Dornsiepen, E.; Weimann, D.P.; Schalley, C.A.; Dehnen, S.; Mehring, M. Impact of the Exchange of the Coordinating Solvent Shell in [Bi₃₈O₄₅(OM_c)₂₄(dmsO)₉] by Alcohols: Crystal Structure, Gas Phase Stability, and Thermoanalysis. *ZAAC* **2018**, *644*, 1796–1804. [[CrossRef](#)]
57. Bhardwaj, R.; Fang, X.; Somasundaran, P.; Attinger, D. Self-assembly of colloidal particles from evaporating droplets: Role of DLVO interactions and proposition of a phase diagram. *Langmuir* **2010**, *26*, 7833–7842. [[CrossRef](#)] [[PubMed](#)]
58. Wypych, G. *Handbook of Solvents*; ChemTec Publishing: Toronto, ON, Canada, 2001.
59. Tolan, M.; Seeck, O.; Schlomka, J.-P.; Press, W.; Wang, J.; Sinha, S.; Li, Z.; Rafailovich, M.; Sokolov, J. Evidence for capillary waves on dewetted polymer film surfaces: A combined X-ray and atomic force microscopy study. *Phys. Rev. Lett.* **1998**, *81*, 2731. [[CrossRef](#)]
60. Mulka, R.; Kujawska, A.; Zajaczkowski, B.; Mancin, S.; Buschmann, M.H. Drying silica-nanofluid droplets. *Colloids Surf. A Physicochem. Eng. Asp.* **2021**, *623*, 126730. [[CrossRef](#)]
61. Witten, T.A.; Sander, L.M. Diffusion-limited aggregation. *Phys. Rev. B* **1983**, *27*, 5686–5697. [[CrossRef](#)]
62. Kotomin, E.A.; Kuzovkov, V.N.; Popov, A.I.; Vila, R. Kinetics of F center annealing and colloid formation in Al₂O₃. *Nucl. Instrum. Methods Phys. Res. B Beam Interact. Mater. At.* **2016**, *374*, 107–110. [[CrossRef](#)]
63. Weber, M. Synthese und Charakterisierung von Bismut(III)-Basierten Halbleitern Ausgehend von Homo- und Heterometallischen Bismutoxidoclustern. Ph.D. Thesis, Technische Universität Chemnitz, Chemnitz, Germany, 2021.